

Data-driven Optimization and Transfer Learning for Cellular Network Antenna Configurations

Mohamed Benzaghta^{*}, Giovanni Geraci^{†*}, David López-Pérez[‡], and Alvaro Valcarce^b

^{*}Univ. Pompeu Fabra, Barcelona, Spain [†]Telefónica Research, Barcelona, Spain

[‡]Univ. Politècnica de València, Spain ^bNokia Bell Labs, Massy, France

Abstract—We propose a data-driven approach for large-scale cellular network optimization, using a production cellular network in London as a case study and employing Sionna ray tracing for site-specific channel propagation modeling. We optimize base station antenna tilts and half-power beamwidths, resulting in more than double the 10%-worst user rates compared to a 3GPP baseline. In scenarios involving aerial users, we identify configurations that increase their median rates fivefold without compromising ground user performance. We further demonstrate the efficacy of model generalization through transfer learning, leveraging available data from a scenario source to predict the optimal solution for a scenario target within a similar number of iterations, without requiring a new initial dataset, and with a negligible performance loss.

I. INTRODUCTION

The large-scale optimization of cellular networks remains a significant challenge due to the complex interdependencies among settings across multiple cells. Coverage and capacity are heavily influenced by the configuration of base station (BS) antennas, with adjustments in parameters such as the tilt angle and half-power beamwidth (HPBW) being critical for optimizing signal strength and minimizing interference. This process, known as cell shaping, becomes increasingly difficult in large-scale networks, as interactions between cells lead to a non-convex and NP-hard optimization problem [1].

The conflicting goals of maximizing both coverage and capacity further complicate cellular network design. Coverage optimization involves directing energy toward cell edges. Capacity optimization prioritizes the signal-to-interference-plus-noise ratio (SINR) for users closer to the cell center. These challenges are exacerbated in scenarios involving nonhomogeneous user distributions, where uniform down-tilt configurations become ineffective [2]–[4].

Traditional methods for optimizing cellular networks, such as those employed in 3GPP frameworks, rely heavily on stochastic simulations and are typically limited to regular

hexagonal deployments [5]. In real networks, site-specific radio frequency planning tools rely on time-consuming trial-and-error methods. A model-based framework for cellular network optimization, based on quantization theory and recently proposed in [6], enables the fine-tuning of antenna parameters for each BS within a given deployment to achieve optimal coverage, capacity, or any trade-off thereof.

In this paper, we propose an alternative approach that leverages available data to maximize real-world key performance indicators (KPIs), which are often mathematically intractable. Our main contributions can be summarized as follows:

Data-driven optimization: We employ high-dimensional Bayesian Optimization (HD-BO) to address a practical large-scale mobile network optimization problem, using a production cellular network in London as a case study. We employ a 3D representation of the area and use Sionna RT [7] to model site-specific channel propagation, considering the actual cell locations and configuration. To evaluate the effectiveness of our data-driven approach, we jointly optimize antenna tilts and HPBWs and identify configurations that achieve more than double the 10%-worst rates with respect to a 3GPP baseline.

Aerial connectivity: In a second case study, we maximize user rates on the ground as well as along 3D aerial corridors for uncrewed aerial vehicle (UAV) users. Ensuring reliable air-to-ground connectivity demands configurations that cannot be easily determined through heuristic methods [8], [9]. Our approach identifies configurations that improve UAV median rates by fivefold, without degrading ground performance.

Transfer learning: In alignment with the 3GPP vision on data-driven model generalization [10], we use transfer learning to leverage knowledge from a previously optimized scenario (*scenario source*), to predict the optimal solution for a new scenario (*scenario target*). We demonstrate that, when the aerial corridor height changes from 140 m–160 m to 40 m–60 m, convergence occurs within a similar number of iterations, without the need for a new initial dataset, and with only a marginal 1% performance decline.

II. SYSTEM MODEL

In this section, we present the network deployment, channel model, and performance metrics utilized in our study.

This work was supported by *a)* the Spanish State Research Agency through grants PID2021-123999OB-I00 and CEX2021-001195-M, *b)* the UPF-Fractus Chair on Tech Transfer and 6G, *c)* the Spanish Ministry of Economic Affairs and Digital Transformation and the European Union NextGenerationEU through actions CNS2023-145384, CNS2023-144333, and the UNICO 5G I+D SORUS project, *d)* the Generalitat Valenciana, Spain, through the CIDEAGENT PlaGenT, Grant CIDEXG/2022/17, Project iTENTE, and *e)* HORIZON-SESAR-2023-DES-ER-02 project ANTENNAE (101167288).

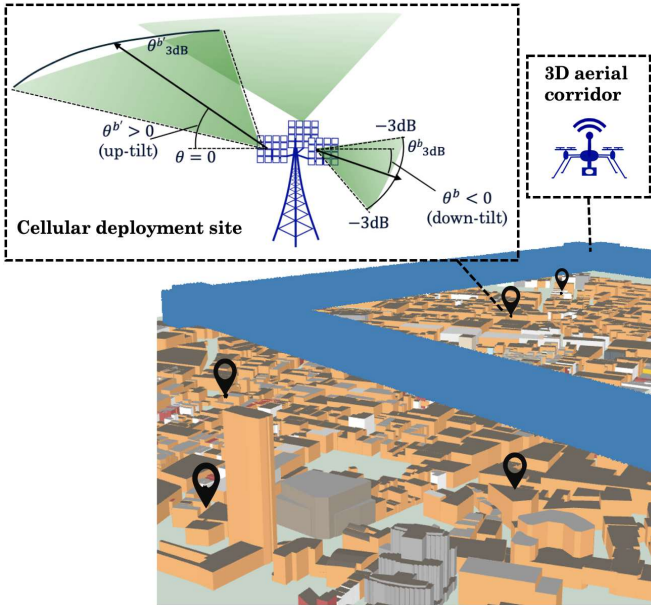


Fig. 1: A section of the area considered, with cell deployment sites indicated by black markers and 3D aerial corridors shown in blue.

Cellular network topology: We consider a site-specific scenario corresponding to a real-world production radio network owned by a leading commercial mobile operator in the UK. The network segment under consideration includes 16 deployment sites, with heights ranging from 22 to 56 meters. Each site consist of three sector antennas, resulting in a total of 48 cells across the network. The geographical area selected for our study covers approximately 1400 m by 1275 m and is situated in London, between latitudes [51.5087, 51.5215] and longitudes [-0.1483, -0.1296]. Fig. 1 illustrates a 3D model of the selected area, highlighting several cell site locations.

Antenna model: We characterize the antenna configuration of each BS b by four main parameters: tilt θ^b , bearing ϕ^b , vertical HPBW θ_{3dB}^b , and horizontal HPBW ϕ_{3dB}^b . The tilt is defined as the angle between the antenna boresight and the horizon and can be electrically adjusted. The bearing indicates the horizontal orientation of each sector. The vertical HPBW is the angular range over which the antenna gain is above half of the maximum gain in the vertical plane, while the horizontal HPBW is the corresponding range in the horizontal plane. In this study, the bearings ϕ^b and the horizontal HPBW ϕ_{3dB}^b are assumed fixed: the former as per the real cellular deployment, the latter set to $\phi_{3dB}^b = 65^\circ$ for all BSs. The tilts θ^b and HPBW θ_{3dB}^b are the object of optimization. The normalized antenna gain for a specific pair of azimuth and elevation, ϕ and θ , between a BS b and a UE k , is [5], and where the maximum antenna gain depends on the HPBW (e.g., $\theta_{3dB}^b = 10^\circ$ and $\phi_{3dB}^b = 65^\circ$ yield a maximum gain of 14 dBi [5]).

$$A(\phi, \theta)_{dB} = -\min\{-[A_H(\phi) + A_V(\theta)], 25\}, \quad (1)$$

where

$$A_H(\phi)_{dB} = -\min\left\{12\left[\frac{(\phi - \phi^b)}{\phi_{3dB}^b}\right]^2, 25\right\}, \quad (2)$$

$$A_V(\theta)_{dB} = -\min\left\{12\left[\frac{(\theta - \theta^b)}{\theta_{3dB}^b}\right]^2, 20\right\}. \quad (3)$$

Site-specific propagation channel: A 3D representation of the selected area is constructed using OpenStreetMap, incorporating terrain and building information. The BSs are positioned and configured according to the actual cellular network topology. The omnidirectional large-scale channel gain (excluding the antenna gain) between BS b and UE k is calculated using Sionna RT [7], a widely-used 3D ray-tracing tool for analyzing site-specific radio wave propagation. Simulations are conducted at a carrier frequency of 2 GHz. The material `itu_concrete` is used to model the permittivity and conductivity of all buildings. The maximum number of reflections and diffractions are set to 5 and 1, respectively. The total large-scale channel gain $G_{b,k}$ is then obtained from the omnidirectional ray tracing channel gain by adding the antenna gain as per (1).

User distribution: We denote by \mathcal{U} the set of users under consideration. User locations are drawn from a desired 3D distribution, e.g., with nonhomogeneous density to model performance prioritization across regions (see Section III-C).

SINR and achievable rates: Through system-level simulations, we compute the downlink SINR in dB experienced by UE k from its serving BS b_k on a given time-frequency physical resource block (PRB), given by

$$\text{SINR}_{dB,k} = 10 \log_{10} \left(\frac{p_{b_k} \cdot G_{b_k,k}}{\sum_{b \in \mathcal{B} \setminus b_k} p_b \cdot G_{b,k} + \sigma_T^2} \right), \quad (4)$$

where σ_T^2 denotes the thermal noise power and p_b denotes the transmit power of BS b on a PRB. The rate \mathcal{R}_k achievable by user k served by BS b_k can be related to its SINR as

$$\mathcal{R}_k = \eta_k B_k \mathbb{E}[\log_2(1 + \text{SINR}_k)], \quad (5)$$

where B_k is the bandwidth allocated to user k , η_k the fraction of time user k is scheduled by the serving BS b_k , and the expectation is taken with respect to the small-scale fading.

Problem formulation: Our goal is to maximize the rates in (5) for all UEs k in the set \mathcal{U} . We define the objective function:

$$f(\boldsymbol{\theta}, \boldsymbol{\theta}_{3dB}) = \sum_{k \in \mathcal{U}} \log \mathcal{R}_k \quad (6)$$

to be maximized with respect to $\boldsymbol{\theta}$ and $\boldsymbol{\theta}_{3dB}$. The vector $\boldsymbol{\theta}$ contains the antenna tilt $\theta^b \in [-90^\circ, 90^\circ]$ of all BSs $b \in \mathcal{B}$, with negative and positive angles denoting down-tilts and up-tilts, respectively. Similarly, the vector $\boldsymbol{\theta}_{3dB}$ contains the HPBW $\theta_{3dB}^b \in [0^\circ, 360^\circ]$ for each BS. While our data-driven approach can be employed to maximize any desired KPI—e.g., any function of the received signal strength, SINR, and rate—we selected the sum-log-rate in (6) due to its widespread use in cellular systems to achieve fairness among users [11].

Maximizing (6) is a complex task since it requires tailoring the cellular deployment to the site-specific signal propagation patterns, while considering inter-cell interference and load balancing. Moreover, the users in \mathcal{U} may be distributed on an arbitrary 3D region with a nonhomogeneous density, thereby requiring performance prioritization across regions.

III. DATA-DRIVEN OPTIMIZATION

We tackle the maximization of (6) through a data-driven Bayesian Optimization (BO) approach. Although BO [12] has previously proven useful in addressing coverage/capacity tradeoffs, optimal radio resource allocation, and mobility management [1], [13]–[18], it faces limitations due to the number of decision variables it can efficiently handle—typically around twenty or fewer in continuous domains [19]. In this paper, we take the first step towards employing high-dimensional BO (HD-BO) for optimizing large-scale cellular networks, thus overcoming the limitations of traditional BO.¹

A. Introduction to Bayesian Optimization

BO is a suitable framework for black-box optimization, where the objective function $f(\cdot)$ is non-convex, non-linear, stochastic, and/or computationally expensive to evaluate. BO operates by iteratively building a probabilistic *surrogate model* of $f(\cdot)$ from previous evaluations at selected query points [12].

We define a query point $\mathbf{x} = [\theta, \theta_{3\text{dB}}]$ as a configuration of the antenna tilts θ^b and vertical HPBW $\theta_{3\text{dB}}^b$ of each BS $b \in \mathcal{B}$, and obtain the corresponding value of $f(\mathbf{x})$ from (6). Since $f(\cdot)$ is a mathematically intractable function—capturing the site-specific propagation channel and the inherent stochasticity of the UE locations—we evaluate $f(\cdot)$ through system-level simulations where the 3D locations of the UEs in \mathcal{U} are sampled at random according to a desired distribution and the channel is generated via Sionna RT. Each evaluation at a point \mathbf{x} yields a noisy sample $\tilde{f}(\mathbf{x})$. In practice, these samples could also be obtained through real-time measurements.

For convenience, let us define $\mathbf{X} = [\mathbf{x}_1, \dots, \mathbf{x}_N]$ as a set of N query points and $\mathbf{f}(\mathbf{X}) = [f_1, \dots, f_N]^\top$ as the set of corresponding evaluations, with $f_i = f(\mathbf{x}_i)$, $i = 1, \dots, N$. We generate an initial dataset $\mathcal{D} = \{\mathbf{x}_1, \dots, \mathbf{x}_{N_0}, \tilde{f}_1, \dots, \tilde{f}_{N_0}\}$ containing N_0 initial observations and constructed according to the model and objective function in Section II. From \mathcal{D} , we use a Gaussian process (GP) prior, $\tilde{f}(\cdot)$, to create a surrogate model (i.e., the posterior) that approximates the objective function, $\tilde{f}(\cdot)$ [12]. The GP model allows to predict the value of $\tilde{f}(\mathbf{x})$ for a query point \mathbf{x} given the previous observations $\tilde{\mathbf{f}}(\mathbf{X}) = \tilde{\mathbf{f}}$ over which the model is constructed. Formally, the GP prior on $\tilde{f}(\mathbf{x})$ prescribes that, for any set of inputs \mathbf{X} , the corresponding objectives $\tilde{\mathbf{f}}$ are jointly distributed as

$$p(\tilde{\mathbf{f}}) = \mathcal{N}(\tilde{\mathbf{f}} \mid \boldsymbol{\mu}(\mathbf{X}), \mathbf{K}(\mathbf{X})), \quad (7)$$

¹While reinforcement learning (RL) is also promising, it tends to require a very large amount of data and to converge slowly. RL also employs random exploration, which in a real production network can lead to test highly suboptimal antenna configurations that degrade the system performance [1].

where $\boldsymbol{\mu}(\mathbf{X}) = [\mu(\mathbf{x}_1), \dots, \mu(\mathbf{x}_N)]^\top$ is the $N \times 1$ mean vector, and $\mathbf{K}(\mathbf{X})$ is the $N \times N$ covariance matrix, whose entry (i, j) is given by the covariance $k(\mathbf{x}_i, \mathbf{x}_j)$. For a point \mathbf{x} , the mean $\mu(\mathbf{x})$ provides a prior knowledge on $\tilde{f}(\mathbf{x})$, while the kernel $\mathbf{K}(\mathbf{X})$ indicates the uncertainty across pairs of values of \mathbf{x} .

Given a set of observed noisy samples $\tilde{\mathbf{f}}$ at previously sampled points \mathbf{X} , the posterior distribution of $\tilde{f}(\mathbf{x})$ at point \mathbf{x} can be obtained as [19]

$$p(\tilde{f}(\mathbf{x}) \mid \mathbf{X}, \tilde{\mathbf{f}}) = \mathcal{N}(\tilde{f}(\mathbf{x}) \mid \mu(\mathbf{x} \mid \mathbf{X}, \tilde{\mathbf{f}}), \sigma^2(\mathbf{x} \mid \mathbf{X}, \tilde{\mathbf{f}})), \quad (8)$$

with

$$\mu(\mathbf{x} \mid \mathbf{X}, \tilde{\mathbf{f}}) = \mu(\mathbf{x}) + \tilde{\mathbf{k}}(\mathbf{x})^\top (\tilde{\mathbf{K}}(\mathbf{X}))^{-1} (\tilde{\mathbf{f}} - \boldsymbol{\mu}(\mathbf{X})), \quad (9)$$

$$\sigma^2(\mathbf{x} \mid \mathbf{X}, \tilde{\mathbf{f}}) = k(\mathbf{x}, \mathbf{x}) - \tilde{\mathbf{k}}(\mathbf{x})^\top (\tilde{\mathbf{K}}(\mathbf{X}))^{-1} \tilde{\mathbf{k}}(\mathbf{x}), \quad (10)$$

where $\tilde{\mathbf{k}}(\mathbf{x}) = [k(\mathbf{x}, \mathbf{x}_1), \dots, k(\mathbf{x}, \mathbf{x}_N)]^\top$ is the $N \times 1$ covariance vector and $\tilde{\mathbf{K}}(\mathbf{X}) = \mathbf{K}(\mathbf{X}) + \sigma^2 \mathbf{I}_N$, with σ^2 denoting the observation noise represented by the variance of the Gaussian distribution, and \mathbf{I}_N denoting the $N \times N$ identity matrix.

An *acquisition function* $\alpha(\cdot)$ (i.e., Thompson sampling) is then employed to score the response from the surrogate model (i.e., the posterior) and determine which point in the search space should be evaluated next.

Traditional BO faces limitations in terms of scalability, due to the limited number of decision variables it can efficiently handle. For the maximization of (6), this constrains the number of antenna parameters that can be jointly optimized.

B. High-dimensional Bayesian Optimization

For BO methods to become more sample-efficient for a larger number of decision variables, it is essential to introduce a hierarchical significance for the dimensions. High-dimensional BO (HD-BO) leverages the fact that certain features may play a crucial role in capturing the behavior of $f(\cdot)$, while others may be of negligible importance.

We employ a state-of-the-art HD-BO method, Trust Region BO (TurBO) [20], to tackle large-scale cellular network design.² TurBO transitions from global surrogate modeling to the management of multiple independent local models, with each model concentrating on a distinct region of the search space. TurBO attains global optimization by simultaneously operating several local models and strategically allocating samples through an implicit multi-armed bandit approach. This enhances the acquisition strategy's effectiveness by focusing samples on promising local optimization endeavors.

TurBO integrates trust region (TR) methods from stochastic optimization, which are gradient-free and utilize simple surrogate models within a defined TR, typically represented as a sphere or polytope centered around the best identified solution. However, these simple surrogate models may necessitate overly small trust regions for precise modeling. To overcome

²We implemented and tested three HD-BO methods: Sparse Axis-Aligned Subspaces (SAASBO) [21, Section 4], BO via Variable Selection (VSBO) [22, Section 3], and Trust Region BO (TurBO) [20, Section 2]. Due to space constraints, our discussion will focus on TurBO, since it demonstrated superior performance and higher suitability for the problem under consideration.

this limitation, TuRBO employs a GP surrogate model within the TR, maintaining essential global BO characteristics such as noise robustness and systematic uncertainty management.

In TuRBO, the TR is defined as a hyperrectangle centered at the current optimal solution, f^* . The side length of the TR is initialized as $L \leftarrow L_{\text{init}}$. Subsequently, the side length for each dimension L_i is adjusted based on its respective length scale λ_i in the GP model. The side length for each dimension is then specified by:

$$L_i = \lambda_i L \cdot \left(\prod_{j=1}^d \lambda_j \right)^{-1/d}. \quad (11)$$

where d is the total number of dimensions (i.e., optimization parameters under consideration). This approach ensures that the TR adapts to the local characteristics of the search space, facilitating more effective optimization in high-dimensional settings.

During each local optimization run, an acquisition function selects a batch of q candidates at each iteration, ensuring they remain within the designated TR. If the TR's side length L were large enough to cover the entire search space, this method would be equivalent to standard global BO. Thus, adjusting L is crucial: the TR needs to be large enough to encompass good solutions but compact enough to ensure the local model's accuracy. The TR is dynamically resized based on optimization progress: it is doubled ($L \leftarrow \min\{L_{\text{max}}, 2L\}$) after τ_{succ} consecutive successes, and halved ($L \leftarrow L/2$) after τ_{fail} consecutive failures. Success and failure counters are reset after adjustments. If L falls below L_{min} , that TR is discarded and a new one is initiated at L_{init} . The TR's side length is capped at L_{max} .

In this study, we run TuRBO using an open-source repository [20] with: $\tau_{\text{succ}} = 3$, $\tau_{\text{fail}} = 15$, $L_{\text{init}} = 0.8$, $L_{\text{min}} = 2^{-7}$, and $L_{\text{max}} = 1.6$. Thompson sampling is used as an acquisition function for selecting candidates both within and across TRs. TuRBO maintains $q = 4$ candidates from the union of all trust regions.

C. Case Studies

To evaluate the effectiveness of our HD-BO approach, we jointly optimize antenna tilts and HPBWs to maximize the sum-log-rate in (6). We study two scenarios, as follows:

Case study #1 — Ground users only: Within the area under consideration, a set \mathcal{G} of ground users (GUEs) are randomly positioned at uniform outdoors (i.e., not within buildings) at a height of 1.5 m, with an average density of 10 GUEs per cell [23]. In this first case study, we set $\mathcal{U} = \mathcal{G}$.

Case study #2 — Ground users and UAV corridors: Besides the set of GUEs \mathcal{G} , we consider a set \mathcal{A} of uncrewed aerial vehicle (UAV) users in four 3D aerial corridors within the area, each measuring 900 m in length, 40 m in width, and positioned at heights between 140 m and 160 m (see Fig. 1). In this second case study, we set $\mathcal{U} = \mathcal{G} \cup \mathcal{A}$, to optimize both GUE and UAV performance. We set the ratio of UAVs to GUEs at 50%, in accordance with 3GPP Case 5 in [23].

TABLE I: System-level parameters for the case studies

Cellular layout	Production radio network, 16 deployment sites at 22–56 m, three sectors per site, one BS per sector
Frequency band	$B_k = 10$ MHz at 2 GHz
Thermal noise	−174 dBm/Hz density
BS max power	46 dBm over the whole bandwidth [5]
User association	Based on received signal strength
User receiver	Omnidirectional antenna
GUE distribution	10 per sector on average, outdoor, at 1.5 m
UAV distribution	Uniform in four aerial corridors at 140–160 m height, 70 UAVs per corridor on average
UAVs/GUEs ratio	50% as per 3GPP Case 5 [23]

Data-driven optimal performance: Fig. 2 presents the cumulative distribution function (CDF) of rates for GUEs (solid) and UAVs (dashed). Black lines represent the performance under the baseline 3GPP configuration, with uniform tilts $\theta^b = -12^\circ$ and vertical HPBW $\theta_{3\text{dB}}^b = 10^\circ \forall b$ [5]. The red line shows the GUE performance after data-driven optimization for GUEs only (case study #1). The blue lines show the performance when optimizing for both GUEs and UAVs (case study #2). The following observations can be made:

- For case study #1, data-driven optimization of tilt and HPBW results in a 120% and 63% improvement in the 10%-tile and median GUE rates, respectively, compared to the 3GPP configuration (solid red vs. solid black).
- For case study #2, under the baseline configuration, 12% of UAVs have data rates below 100 kbps, the minimum requirement set by 3GPP for command and control links [23] (dashed black).³ Data-driven optimization increases UAV rates nearly fivefold in both the 10%-tile and median (dashed blue vs. dashed black).
- For case study #2, the improvement in UAV performance does not lead to a significant GUE performance degradation. The 10%-tile GUE rates are only 17% lower than those optimized for GUEs only (solid blue vs. solid red) and are still 82% higher than the baseline 3GPP configuration (solid blue vs. solid black). This demonstrates the capability of the data-driven approach to identify optimal trade-offs across the 3D user region, encompassing ground and aerial users.

Data-driven optimal configuration: Fig. 3 and Fig. 4 show the optimal configurations of antenna tilts θ and HPBWs $\theta_{3\text{dB}}$ for the two case studies. Each index denotes the deployment site with three sectors. We note the following:

- In case study #1, as shown in Fig. 3, the optimal data-driven configuration (green dots) deviates significantly from the uniform 3GPP baseline (black squares), with BSs exhibiting varied tilts and often wider HPBWs than the baseline 10° . This setup, tailored to the irregular urban deployment, leads to the performance gains highlighted in Fig. 2.
- In case study #2, Fig. 4 uses markers to differentiate between cells serving GUEs (green circles) and UAVs (blue

³While the Shannon rates in (5) are always non-zero, 80% of the UAVs have SINRs below −5 dB: a proxy for outage [24]. The optimal tilt and HPBW configuration reduces this outage from 80% to zero.

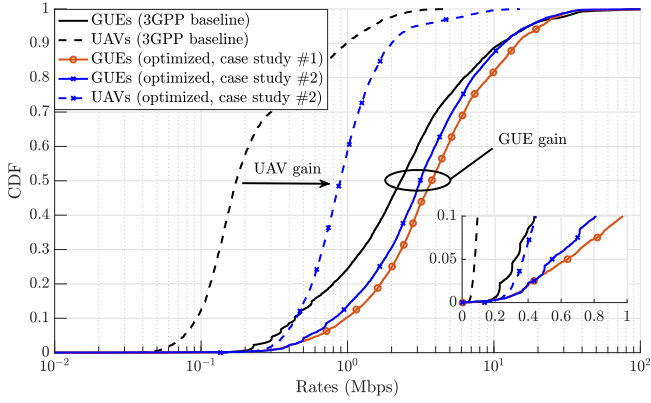


Fig. 2: Rates achieved by GUEs and UAVs when the network is optimized for GUEs only (case study #1), GUEs and UAV corridors (case study #2), and with a 3GPP baseline configuration.

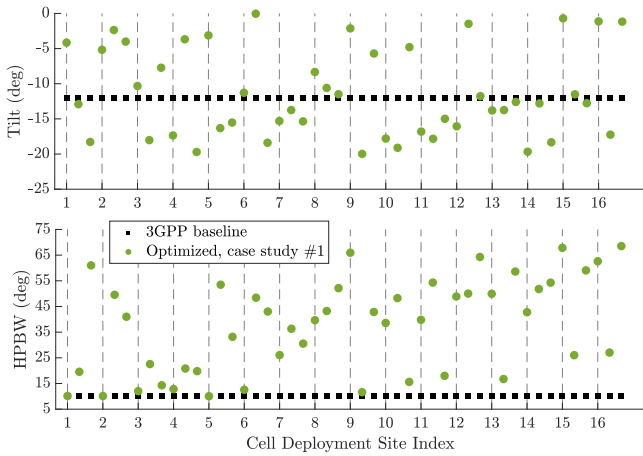


Fig. 3: Optimal tilts and HPBW for case study #1, with GUEs only.

diamonds). Unlike case study #1, where all BSs are down-tilted, optimizing for both GUEs and UAVs results in 22 BSs being up-tilted, with the remaining BSs down-tilted. While 18 BSs in Fig. 3 have down-tilted angles below -15° , all down-tilted BSs in Fig. 4 maintain angles above -15° , effectively filling the coverage gaps left by the up-tilted BSs. Overall, the non-trivial optimal configurations of tilts and HPBW, particularly in case study #2, reflect the complexity of achieving the best performance trade-offs.

IV. TRANSFER LEARNING

The commercial adoption of a machine learning model requires consistent performance across various scenarios [25]. In this section, we explore the generalization capabilities of the HD-BO framework across different UE distributions, within the context of *transfer learning*.

Scenario source vs. scenario target: Transfer learning in optimization utilizes knowledge or data from a previously solved problem (*source*) to expedite the solution of a new but related problem (*target*). This method proves especially advantageous when generating the initial dataset \mathcal{D} required

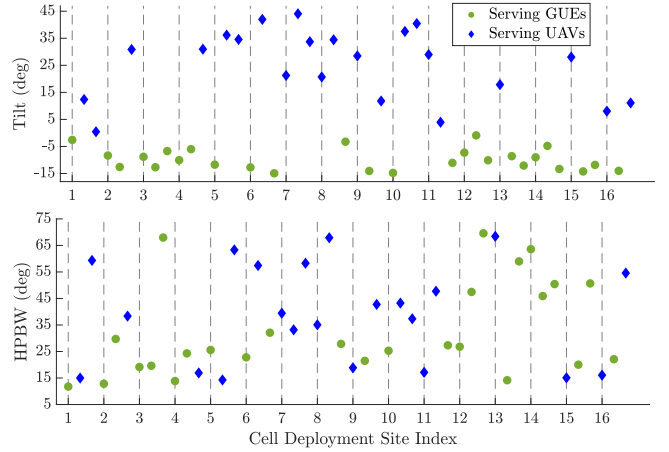


Fig. 4: Optimal tilts and HPBW for case study #2. Green circles and blue diamonds denote BSs serving GUEs and UAVs, respectively.

for the BO posterior is costly or time-consuming, e.g., because it requires measurements. Let \mathcal{D}_{sr} and \mathcal{D}_{tg} denote initial datasets obtained for scenarios source and target, respectively. We conduct three evaluations, varying the percentage of the initial dataset \mathcal{D} that is based on scenario target, as follows:

- 100% ($\mathcal{D} = \mathcal{D}_{\text{tg}}$, prior knowledge based on scenario target).
- 50% (half of \mathcal{D} is drawn from \mathcal{D}_{sr} , half is from \mathcal{D}_{tg}).
- 0% ($\mathcal{D} = \mathcal{D}_{\text{sr}}$, prior knowledge based on scenario source).

We apply *scenario-specific* transfer learning to case study #2, where our objective is to utilize data collected from applying data-driven optimization to a particular UAV corridors height to a new scenario where the height has changed. The scenario source is based on the previously described case study #2, consisting of GUEs and UAVs along 3D aerial corridors at an altitude between 140 m–160 m. The scenario target changes the aerial corridors height to 40 m–60 m.

Convergence of transfer learning: Fig. 5 illustrates the convergence of transfer learning using HD-BO, showing the best observed objective at each iteration n . To show a quantity of practical interest, we plot the geometrical mean rate across all UEs in \mathcal{U} , closely related to the objective function $f(\cdot)$ in (6) as follows:

$$\bar{\mathcal{R}} = \left(\prod_{k \in \mathcal{U}} \mathcal{R}_k \right)^{\frac{1}{|\mathcal{U}|}} = e^{f(\cdot)/|\mathcal{U}|}, \quad (12)$$

where $|\mathcal{U}|$ denotes the cardinality of the UE set. The initial dataset \mathcal{D} contains $N_o = 200$ observations drawn from \mathcal{D}_{sr} (blue), from \mathcal{D}_{tg} (green), or half each (red). Successive samples are collected on the target scenario (x-axis). Fig. 5 shows that with a 50%/50% reliance on $\mathcal{D}_{\text{tg}}/\mathcal{D}_{\text{sr}}$, convergence occurs in a comparable number of iterations to that observed with 100% reliance on \mathcal{D}_{tg} (i.e., without transfer learning). This shows that resources can be conserved when generating the initial dataset \mathcal{D} , highlighting the HD-BO posterior’s capability to generalize after completing an optimization run for a related task. Even without prior knowledge of the target ($\mathcal{D} = \mathcal{D}_{\text{sr}}$), performance declines by just 1%.

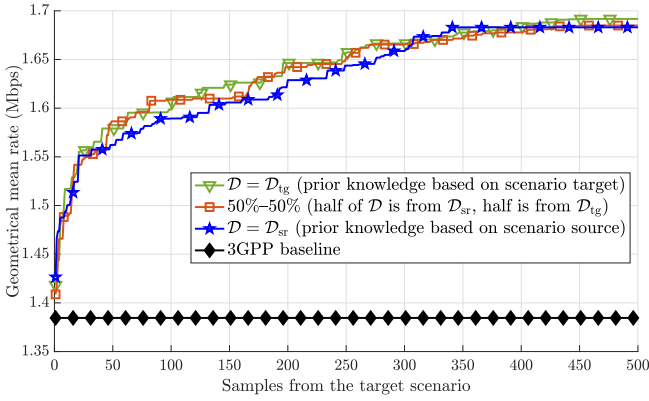


Fig. 5: Convergence of transfer learning applied on case study #2. The initial dataset \mathcal{D} contains $N_0 = 200$ observations.

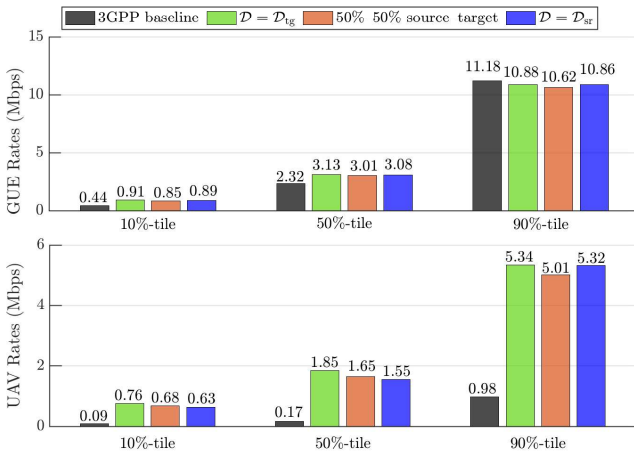


Fig. 6: Performance of transfer learning applied on case study #2.

Performance of transfer learning: Fig. 6 shows the effectiveness of transfer learning in terms of achievable rates. Similarly to case study #2, this figure shows that data-driven optimization of tilts and HPBW significantly improves the UAV rates when these are distributed along aerial corridors of between 40 m and 60 m in height, with an order of magnitude gain in median UAV rates and 35% gains in median GUE rates (green vs. gray). Importantly, under full transfer learning, the UAVs median rate is only reduced by 16% compared to data-driven optimization without transfer learning, while the GUE median rate is nearly preserved (blue vs. green).

V. CONCLUSION

We employed data-driven optimization to jointly configure the BS antenna tilts and HPBWs of a real-world cellular network, achieving more than double the 10%-worst rates with respect to a 3GPP baseline. For scenarios involving UAVs, we identified configurations that improve their median rates fivefold, without degrading ground UE performance. We further explored the transfer learning capabilities of our approach, using data from a scenario source to predict the optimal solution for a scenario target, reaching convergence

with a similar number of iterations and negligible loss, without requiring a new initial dataset.

This work calls for multiple extensions. The parameters being optimized could include cell-specific beam codebook configurations or mobility management thresholds. The objective function maximization could be generalized to a multi-objective Pareto front: a set of non-dominated solutions where no objective can be improved without compromising another.

REFERENCES

- [1] E. Tekgul *et al.*, “Joint uplink-downlink capacity and coverage optimization via site-specific learning of antenna settings,” *IEEE Trans. Wireless Commun.*, 2024.
- [2] G. Geraci *et al.*, “What will the future of UAV cellular communications be? A flight from 5G to 6G,” *IEEE Commun. Surveys Tuts.*, vol. 24, no. 3, pp. 1304–1335, 2022.
- [3] G. Geraci *et al.*, “Integrating terrestrial and non-terrestrial networks: 3D opportunities and challenges,” *IEEE Commun. Mag.*, 2023.
- [4] M. Benzaghta *et al.*, “UAV communications in integrated terrestrial and non-terrestrial networks,” in *Proc. IEEE Globecom*, 2022, pp. 3706–3711.
- [5] 3GPP Technical Report 36.814, “Evolved Universal Terrestrial Radio Access (E-UTRA); Further advancements for E-UTRA physical layer aspects,” Mar. 2017.
- [6] S. Karimi-Bidhendi *et al.*, “Optimizing cellular networks for UAV corridors via quantization theory,” *IEEE Trans. Wireless Commun.*, 2024.
- [7] J. Hoydis *et al.*, “Sionna RT: Differentiable ray tracing for radio propagation modeling,” *arXiv:2303.11103*, 2023.
- [8] S. J. Maeng *et al.*, “Base station antenna up tilt optimization for cellular-connected drone corridors,” *IEEE Trans. Aerospace Elec. Sys.*, 2023.
- [9] M. Bernabè *et al.*, “Massive MIMO for aerial highways: Enhancing cell selection via SSB beams optimization,” *IEEE Open Journal of the Communications Society*, vol. 5, pp. 3975–3996, 2024.
- [10] 3GPP TR 38.843, “Study on artificial intelligence (AI)/machine learning (ML) for NR air interface (Release 18),” Jun. 2023.
- [11] F. P. Kelly *et al.*, “Rate control for communication networks: Shadow prices, proportional fairness and stability,” *Journal of the Operational Research society*, vol. 49, pp. 237–252, 1998.
- [12] B. Shahriari *et al.*, “Taking the human out of the loop: A review of Bayesian optimization,” *Proc. IEEE*, vol. 104, no. 1, pp. 148–175, 2015.
- [13] R. M. Dreifuerst *et al.*, “Optimizing coverage and capacity in cellular networks using machine learning,” in *Proc. IEEE ICASSP*, 2021, pp. 8138–8142.
- [14] Y. Zhang *et al.*, “Bayesian and multi-armed contextual meta-optimization for efficient wireless radio resource management,” *IEEE Trans. on Cognitive Communications and Networking*, 2023.
- [15] L. Maggi *et al.*, “Bayesian optimization for radio resource management: Open loop power control,” *IEEE J. Sel. Areas Commun.*, vol. 39, no. 7, pp. 1858–1871, 2021.
- [16] S. S. Tambovskiy *et al.*, “Cell-free data power control via scalable multi-objective Bayesian optimisation,” in *Proc. IEEE PIMRC*, 2022, pp. 1–6.
- [17] E. de Carvalho *et al.*, “Towards mobility management with multi-objective Bayesian optimization,” in *Proc. IEEE WCNC*, 2023, pp. 1–6.
- [18] M. Benzaghta *et al.*, “Designing cellular networks for UAV corridors via Bayesian optimization,” in *Proc. IEEE Globecom*, 2023, pp. 4552–4557.
- [19] P. I. Frazier, “A tutorial on Bayesian optimization,” *arXiv:1807.02811*, 2018.
- [20] D. Eriksson *et al.*, “Scalable global optimization via local Bayesian optimization,” *NeurIPS*, vol. 32, 2019.
- [21] D. Eriksson and M. Jankowiak, “High-dimensional Bayesian optimization with sparse axis-aligned subspaces,” in *Uncertainty in Artificial Intelligence*. PMLR, 2021, pp. 493–503.
- [22] Y. Shen and C. Kingsford, “Computationally efficient high-dimensional Bayesian optimization via variable selection,” *arXiv:2109.09264*, 2021.
- [23] 3GPP TR 36.777, “Study on enhanced LTE support for aerial vehicles (Release 15),” Dec. 2017.
- [24] G. Geraci *et al.*, “Understanding UAV cellular communications: From existing networks to massive MIMO,” *IEEE Access*, 2018.
- [25] X. Lin, “An overview of the 3GPP study on artificial intelligence for 5G new radio,” *arXiv:2308.05315*, 2023.